Refinement of particle detection by the hybrid method in digital in-line holography

Jian Gao,[1] Daniel R. Guildenbecher,[2] Luke Engvall,[3] Phillip L. Reu,[2] and Jun Chen[1,*]

[1]School of Mechanical Engineering, Purdue University, West Lafayette, Indiana 47907, USA

[2]Sandia National Laboratories, Albuquerque, New Mexico 87185, USA

[3]Department of Mechanical Engineering, University of Colorado at Boulder, Colorado 80309, USA

*Corresponding author: junchen@purdue.edu

Received 8 May 2014; revised 1 July 2014; accepted 2 July 2014; posted 3 July 2014 (Doc. ID 211710); published 7 August 2014

Digital in-line holography provides simultaneous particle size and three-dimensional position measurements. In general, the measurement accuracy varies locally, and tends to decrease where particles are closely spaced, due to noise resulting from diffraction by adjacent particles. Aggravating the situation is the identification of transversely adjoining particles as a single particle, which introduces significant errors in both size and position measurements. Here, we develop a refinement procedure that distinguishes such erroneous particles from accurately detected ones and further separates individual particles. Effectiveness of the refinement is characterized using simulations, experimental holograms of calibration fields, and a few practical applications to liquid breakup. Significant improvements in the accuracy of the measured particle sizes, positions, and displacements confirm the usefulness of the proposed method. © 2014 Optical Society of America

OCIS codes: (090.1995) Digital holography; (120.0120) Instrumentation, measurement, and metrology; (100.6890) Three-dimensional image processing; (350.4990) Particles.

http://dx.doi.org/10.1364/AO.53.00G130

1. Introduction

Particle detection is one important application of digital in-line holography (DIH), which provides particle size and relative position measurements. DIH is advantageous due to its simple optical configuration and unique access to three-dimensional (3D) information. Specifically, 3D spatial coordinates and the size distribution of particles in a volume can be determined from a single hologram. Furthermore, 3D trajectories and velocities can be extracted from sequential holograms via particle matching. The literature contains many applications to solid particles [1–4], liquid or gaseous particles [5–10], and biological particles [11,12], where particle sizes range from a few to hundreds of micrometers. Note, in order to resolve small particles [9] or to expand the field of view (FOV) [13], magnification is usually introduced by a lens added in the optical path. Here, we focus on lens-less applications, although the proposed method may be readily extended to the magnified configuration.

A general setup of DIH for particle detection is shown in Fig. 1(a), where a collimated beam illuminates the particles. The forward-scattered light from the particles (object light) and the undisturbed part of the illuminating beam (reference light) interfere at the imaging sensor. The intensity pattern of the interference is recorded as the in-line hologram, $h(x,y)$, in which the particle size and distance information is encoded in the interference fringes. An example particle hologram is shown in Fig. 1(b), which is taken from the synthetic holograms described

1559-128X/14/27G130-09$15.00/0

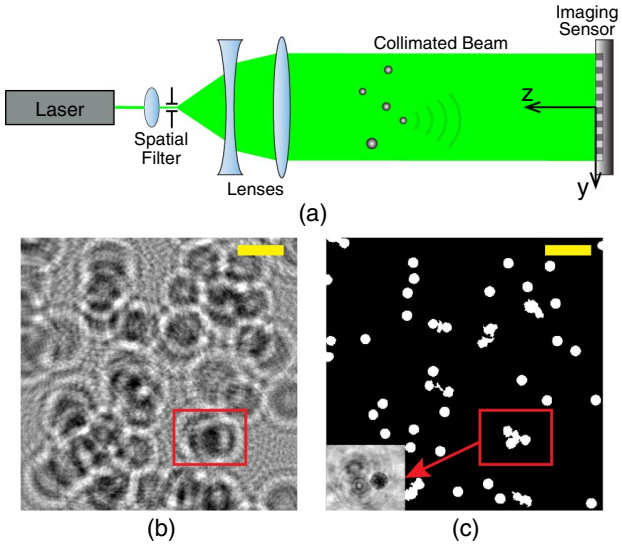

Fig. 1. (a) Experimental setup of DIH, (b) a portion of a particle hologram taken from the synthetic holograms described in Subsection 4.A, and (c) particle 2D morphology extracted by the hybrid method. Inset in (c): image reconstructed at the detected z position of the false particle enclosed in the red rectangle. Notice, no particles appear in-focus. The scale bars represent 0.5 mm.

in Subsection 4.A. In numerical reconstruction/refocusing, the complex amplitude, E, of the reconstructed wave is evaluated by

$$E(x,y,z) = \mathcal{F}^{-1}\{\mathcal{F}\{h(x,y)\} \cdot G(f_x,f_y,z)\}. \quad (1)$$

$$G(f_x,f_y,z) = \exp\left[j\frac{2\pi z}{\lambda}\sqrt{1-(\lambda f_x)^2-(\lambda f_y)^2}\right] \quad (2)$$

is the Fourier transform of the Rayleigh–Sommerfeld diffraction kernel [14]. f_x and f_y are coordinates in the spatial frequency domain. λ is the wavelength. $\mathcal{F}$ and $\mathcal{F}^{-1}$ denote the Fourier transform and inverse Fourier transform, respectively. Symbol "$\cdot$" denotes point-wise multiplication. The reconstructed amplitude is $A = |E|$, and the reconstructed intensity is $I = |E|^2$. z is the reconstruction distance, which is the numerical propagation distance from the hologram plane ($z = 0$) to the image plane, as shown in Fig. 1(a).

2. Background

Numerous hologram processing methods have been developed to extract particle information, especially the out-of-plane (z) position of a particle [15]. To determine z, methods often utilize the fact that the reconstructed image of a particle is the most distinct when z is equivalent to the physical distance between the particle and the hologram plane [15]. After locating the z-depth, the size, two-dimensional (2D) morphology, and in-plane (x–y) position of particles can be retrieved via image analysis.

Due to the nature of the in-line configuration, as the number of particles increases in the FOV of DIH, the quality of the hologram degrades due to the reduction of reference light and the reciprocal effects of scattering from multiple particles. Therefore, in general DIH measurement accuracy decreases at higher particle number density. In addition to this, even at relatively sparse conditions, particle closeness in the x–y plane can be a major source of measurement error. This is because transversely adjoining (overlapping) particles are prone to be identified as single particles by the extraction algorithms. For example, the false particle (connected binary segment) encircled in Fig. 1(c) actually contains three particles. Consequently, the detected size is about three times the actual size, and the detected z position is also erroneous, as shown in the inset in Fig. 1(c). As this example illustrates, false identification results in errors in both particle size and position measurements [5,16,17].

Here, a false particle is defined as a detected particle that does not correspond to exactly one particle in the actual particle field. Since spaced distribution of particles is typically not guaranteed, false particles occur even in measurements of very sparse particle fields. Therefore, this is a common problem that degrades the accuracy of many DIH measurements, and thus methods to diagnose and correct false particles are warranted. Various image processing techniques for the separation of overlapping objects have been developed in the computer vision community [17]. Generally, these techniques are designed specifically for objects lying approximately in the same transverse plane such that all objects appear in-focus. In contrast, in DIH overlapping particles often reside in different z-planes within a volume. Therefore, the computer vision techniques are generally ill-suited, and further work is needed to develop particle separation techniques specific to DIH.

The literature contains a few methods to recognize false particles and segment neighboring particles in DIH. For example, Tian *et al.* [5] use a Gaussian mixture model (GMM) to resolve the depth distribution of the edge pixels of a false particle in order to determine the number and depths of component particles. While the results in [5] appear promising, few details are given on the method implementation, and our own initial efforts to utilize a GMM indicate high sensitivity to noise. In another example, Lamadie *et al.* [8] apply a Euclidean distance transform (EDT) directly to particle diffraction patterns in order to identify adjacent particles. Successful implementation of a EDT depends on the similarity of the images of overlapping objects, as indicated in its application to nucleus counting in microscope images [18,19]. Therefore, this method is limited to similar-size particles, whose separation in the z direction is small enough so that their diffraction patterns are similar. Finally, Mallahi and Dubois [17] propose extracting the depths of component regions around a particle segment border and analyzing the plateaus of the depth distribution to determine the number and depths of overlapping particles. This method is proposed for application in digital holographic microscopy where magnified

particle images are processed. Accordingly, it is less effective in separating particles in unit-magnification holograms because of the difficulty in extracting the depth plateaus from a less resolved particle image.

In this work, we develop a refinement method to identify and correct erroneous particles (mostly caused by transverse closeness). The proposed method serves as a complementary procedure for the hybrid method that we proposed in [20]. Here, particle refinement is realized by analyzing peaks in a sharpness profile as a function of z for each initially detected particle and applying the hybrid method at the valid peaks. To characterize the performance of the refinement method, it is applied to simulated holograms, experimental holograms of calibration fields, and a few practical applications to liquid breakup. It is shown that the measurement accuracy is significantly improved with the refinement.

3. Methodology

A. Hybrid Method

The hybrid method [20] is proposed as a hologram processing algorithm to extract the particle information (size and 3D spatial coordinate) encoded in a hologram. The particle field is first segmented via thresholding a minimum intensity map using a threshold that is automatically selected through maximization of a global edge sharpness. Next, optimal thresholds are determined for individual particle segments in order to obtain binary particle images. Finally, the size and x–y coordinates are extracted from the binary image of each particle, and the z-coordinate is determined from the average depth of the edge pixels. Advantages of the hybrid method include automatic selection of segmentation thresholds, applicability to arbitrary-shaped particles, and demonstrated accuracy. A detailed description of the hybrid method can be found in [15], and applications are available in [9,10].

B. Refinement of Particle Measurement

The proposed refinement procedure consists of identification followed by separation of false particles. First, a sharpness profile is calculated for each measured particle, and this profile is analyzed in order to determine if the measured particle is a false particle. Next, particle separation is performed for false particles, and the original measurement is replaced with that obtained from the separation.

1. *Identification of False Particles*

Particles that appear transversely adjoining (overlapping) in the x–y plane may lie in distinctly different z-positions. To detect such particles, we propose a sharpness profile that quantifies the edge sharpness within a region that has been initially identified to contain a particle. Sharpness profiles that display multiple peaks throughout the z-direction are theorized to be indicative of transversely adjoining and falsely detected particles.

The sharpness profile is expressed as

$$S(z) = \frac{\sum_{k,l\in W} \mathcal{E}\{\mathcal{T}_{t(z)}\{I(k,l,z)\}\} \cdot T(k,l,z)}{\sum\limits_{k,l\in W} \mathcal{E}\{\mathcal{T}_{t(z)}\{I(k,l,z)\}\}}, \quad (3)$$

where (k,l) are discretized coordinates in the x–y directions. W is the set of pixels enclosed by a window around the initially identified particle. $t(z)$ is the edge-sharpness-maximizing threshold determined automatically by the method described in [15,20]. Note, $t(z)$ is recalculated at each z, and therefore varies at different depths. $T(k,l,z)$ is the quantified sharpness image, which can be expressed as

$$T(k,l,z) = [A(k,l,z) \otimes K_x]^2 + [A(k,l,z) \otimes K_y]^2, \quad (4)$$

where $\otimes$ denotes the convolution operation, and K_x and K_y are the horizontal and vertical Sobel kernels, respectively. Symbol $\mathcal{T}_t\{\}$ denotes the thresholding operation using a threshold, t, which results in a binary image. Symbol $\mathcal{E}\{\}$ denotes an operation that extracts the exterior and interior edge pixels of binary segments, and the output is also a binary image [15]. The numerator in Eq. (3) is the sum of edge sharpness obtained at the optimal threshold, $t(z)$, and the denominator is the total number of edge pixels.

Based on Eq. (3), the sharpness profile of the false particle encircled in Fig. 1(c) is obtained, as shown in Fig. 2. Multiple local maximums exist in the profile, and only a few valid peaks correspond to focused particles. Consequently, criteria must be defined to differentiate valid peaks from background noise in the sharpness profile. By trial and error, several criteria combined together are found effective in selecting valid peaks, as indicated in Fig. 2. Specifically, the heights of valid peaks are required to be greater than 60% of the maximum value. Also, the peak width is quantified as the width when the focus metric ($S(z)$) drops to 80% of the peak value. Using this it is required that a valid peak should have a width less than 20 times the mean particle diameter initially determined by the hybrid method. The establishment of these criteria minimizes the need for manual inputs in the algorithm and facilitates automatic implementation of the refinement procedure. Using this method, three valid peaks are detected in Fig. 2.

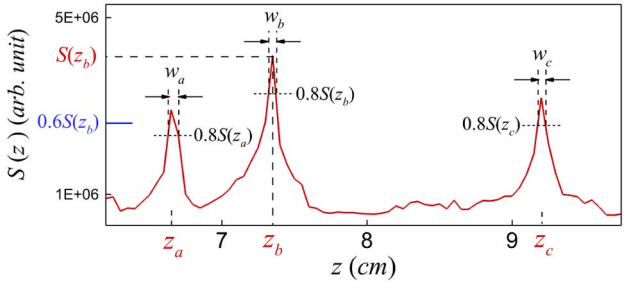

Fig. 2. Sharpness profile of the false particle encircled in Fig. 1(c).

The intensity images reconstructed at the z-positions of each valid peak, corresponding sharpness images, and extracted binary images are shown in Fig. 3. In this example, the peak z-position is shown to provide an accurate measurement of the particle depth.

Finally, a particle whose sharpness profile has less than or more than one valid peak is identified as a false particle. In addition, for an accurately detected particle, the initial z-position is expected to be close to the peak z-position in the sharpness profile. Excessive discrepancy between the initially detected z-position and the peak z-position is indicative of potential measurement errors. Therefore, a particle with a discrepancy larger than 5 times the particle diameter is also diagnosed as a false particle.

2. *Separation of Particles*

Adjoining (overlapping) particles in a false particle can be separated when the overlapping area is small and the particles are significantly separated in the z direction. In that case, thresholding the intensity images reconstructed at valid peaks using the optimal thresholds gives well-separated (non-overlapping) particles, as demonstrated in Figs. 3(g)–3(i). Here the sizes and in-plane positions are accurately determined from the separated binary particle images.

However, for certain particles, thresholding is unable to detach neighboring particles. For example, Fig. 4(a) displays the sharpness profile of a false particle [Fig. 4(j)], from which two valid peaks are detected. Unlike the case in Fig. 3, particle images obtained at each valid peak [Figs. 4(d) and 4(h)] still retain the false overlap. Nevertheless, the sharpness images at the two valid peaks [Figs. 4(c) and 4(g)]

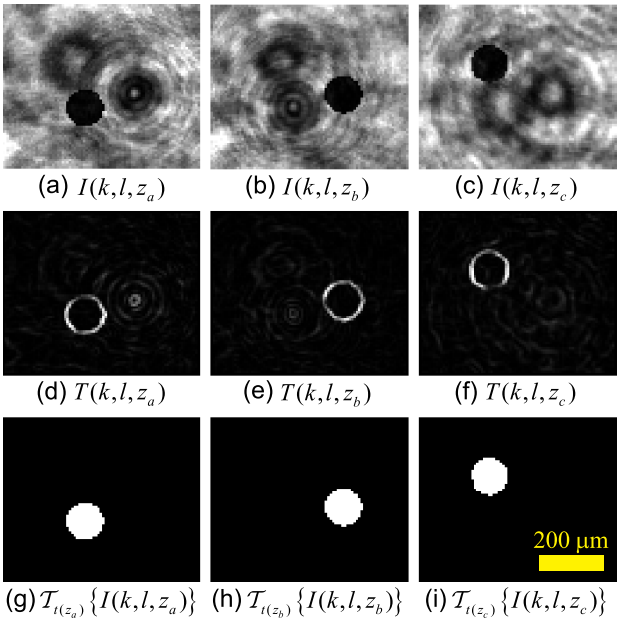

Fig. 3. (a)–(c) Intensity images reconstructed at the valid peaks in Fig. 2, (d)–(f) corresponding sharpness images, and (g)–(i) extracted binary images of particles a, b, and c.

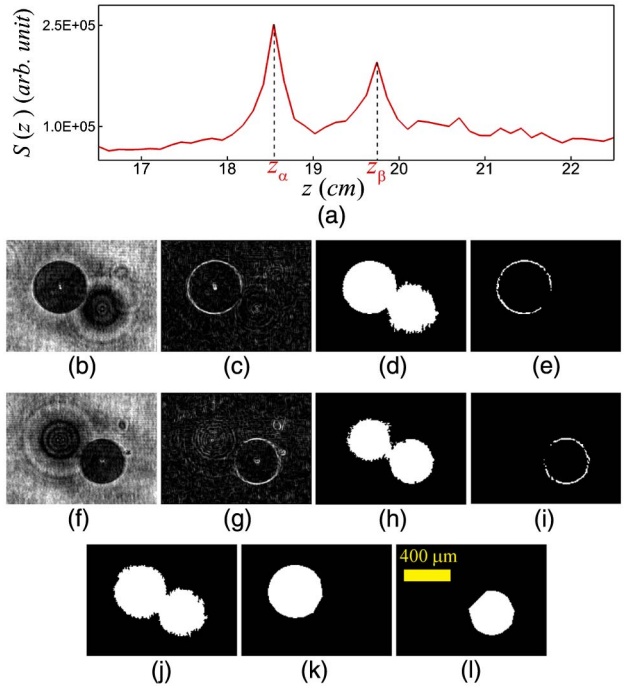

Fig. 4. (a) Sharpness profile of the false particle in (j), (b) $I(k,l,z_\alpha)$, intensity image reconstructed at z_α, (c) $T(k,l,z_\alpha)$, sharpness image at z_α, (d) $\mathcal{T}_{t(z_\alpha)}\{I(k,l,z_\alpha)\}$, initially extracted particle 2D morphology at z_α, (e) extracted edge pixels of particle α, (f) $I(k,l,z_\beta)$, intensity image reconstructed at z_β, (g) $T(k,l,z_\beta)$, sharpness image at z_β, (h) $\mathcal{T}_{t(z_\beta)}\{I(k,l,z_\beta)\}$, initially extracted particle 2D morphology at z_β, (i) extracted edge pixels of particle β, (j) initial false particle, (k) separated particle α, and (l) separated particle β.

show two distinct regions that correspond to the particle edges. To separate the two particles, we choose to investigate the distribution of sharpness along the edges of each detected region in Figs. 4(d) and 4(h). Here, the sum of the sharpness values along the edge pixels is defined as the total edge sharpness. All edge pixels are selected for which 60% of the total edge sharpness is contributed by pixels of greater sharpness. Using this criterion, the edge pixels shown in Figs. 4(e) and 4(i) are selected. Finally, the edge pixels are connected by a morphological dilation operation along the particle edge, followed by a convex hull operation to "close" the edge and form a particle image, as shown Figs. 4(k) and 4(l). Note, for spherical particles, the properties of a circle can be utilized to recover the complete particle image from the edge pixels [21]. Here, the convex hull operation is used to provide a general recovery solution.

4. Results and Discussion

In this section, the refinement is applied to simulated holograms, experimental holograms of calibration fields, and a few practical applications to liquid breakup. The goals are to examine the performance with respect to false particle identification, overlapping particle separation, and effects on measurement accuracy.

A. Application to Synthetic Holograms

In simulated holograms, all relevant particle properties are known, including the size, 3D position, and z-displacement. Here, improvement in measurement accuracy, achieved after refinement, is characterized quantitatively via comparison with these quantities.

The synthetic particle field consists of a mixture of circular particles of two diameters (115 and 450 μm) randomly distributed in a volume of dimensions 7.6 mm × 7.6 mm × 5 cm, where 5 cm is the dimension in the z direction. In total there are 287 particles in the particle field, and the number ratio of smaller particles to bigger particles is 50:1. The hologram size is 1024 × 1024 with 7.4 μm × 7.4 μm pixels. The wavelength is 532 nm. The distance between the hologram plane and the nearest particle, L, is set to 6.5 and 18.5 cm.

Five holograms of randomly distributed particles are simulated at each L using the method described in [15]. Next, the 10 holograms are processed using the hybrid method to extract initial particle information. Then the results are refined using the procedure described in Subsection 3.B. Note, for $L = 6.5$ cm, particles within 50 pixels of the hologram borders are neglected; for $L = 18.5$ cm, the border rejection size is 100 pixels. This is necessary to reduce the effects of fringe loss near the hologram borders.

The refinement successfully identifies and separates many false particles as demonstrated in Fig. 5. Compared with the actual particle field [Fig. 5(b)], results obtained before refinement [Fig. 5(c)] have significant size and depth errors. After refinement, however, most false particles are corrected, as shown in Fig. 5(d).

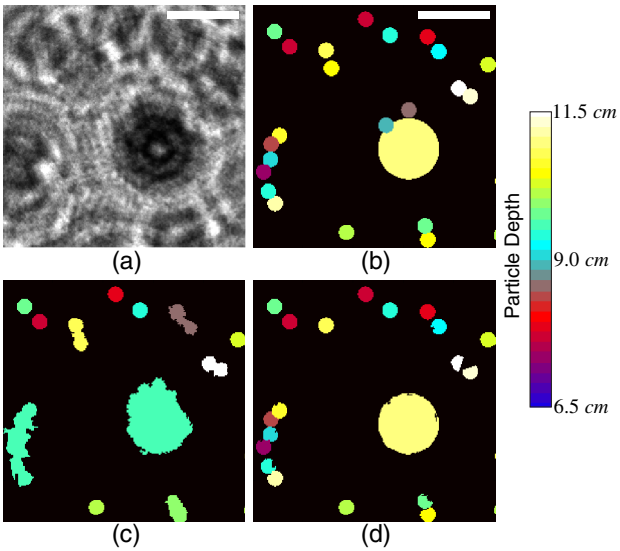

Fig. 5. (a) Portion of a synthetic hologram at $L = 6.5$ cm, (b) actual particle image with color indicating the particle depth, (c) particle image obtained before refinement with color indicating the measured particle depth, and (d) particle image obtained after refinement with color indicating the measured particle depth. The scale bars represent 0.5 mm.

Several parameters are used to characterize the particle field and to evaluate the performance of the refinement. $\overline{F}$ is the average Fresnel number defined in [15]. The shadow density [8,22], SD, is the ratio of the sum of particle cross-section areas to the cross-section area of the hologram. It is a parameter that measures the particle number density. To achieve sufficient hologram quality (signal-to-noise ratio) for particle detection, it is theorized that the shadow density should not exceed 10% [8,22]. Moreover, as the shadow density increases, the particles tend to overlap more severely, which adds to the difficulty in identifying and separating them. Detection effectiveness, R_d, is the ratio of the number of detected particles to the actual number of particles, where the prime signifies quantities obtained after refinement. N_f is the total number of false particles, determined via manual inspection of the results. Identification effectiveness, R_i, is the ratio of the number of identified false particles to the total number of false particles. Finally, separation effectiveness, R_s, is the ratio of the number of successful separations to the number of identified false particles. In a successful separation, the number of separated particles is equal to the actual number of particles.

The performance parameters of the refinement are listed in Table 1. The data are obtained from five realizations for each L. It is revealed that about 90% of the false particles are identified, and the majority of them are successfully separated. Correspondingly, the detection effectiveness, R_d, is increased after refinement. Adverse conditions, such as close spacing in the z direction, particle size difference, excessive overlapping area (>50%), and multiple (>3) attached particles, decrease the effectiveness of particle refinement. Nevertheless, these extreme conditions are rare in a randomly distributed particle field of moderate density (SD < 10%), and thus most of the false particles can be identified and separated.

The correction of false particles significantly improves the measurement accuracy, as shown in Fig. 6. Before the refinement, only 80% of the detected particles have depth errors smaller than 5 times the particle diameter, whereas after the refinement,

Table 1. Performance of the Refinement Applied to Synthetic Holograms

		$L = 6.5$ cm, $\overline{F} = 0.076$, SD = 6.7%	$L = 18.5$ cm, $\overline{F} = 0.033$, SD = 6.7%
Detection Effectiveness	R_d	75.9%	75.4%
	R'_d[a]	88.0%	85.5%
Number of false particle N_f		171	133
Identification effectiveness R_i		92.4%	88.0%
Separation effectiveness R_s		74.1%	68.4%

[a]The prime signifies quantities obtained after refinement.

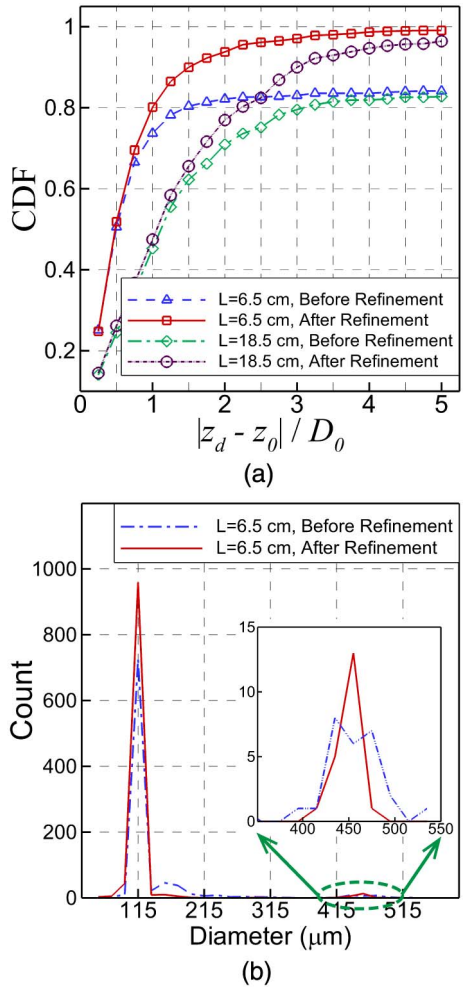

Fig. 6. Improvement in z-position and size accuracy achieved by the refinement applied to synthetic holograms. (a) Cumulative distribution function (CDF) of relative depth error. (b) Measured particle size distribution. z_d, determined particle depth; z_0, actual particle depth; D_0, actual particle diameter.

the percentage is increased to about 95%. In addition, the size distribution measured with the refinement concentrates better at the actual sizes (115 and 450 μm). The results obtained from farther particle fields ($L = 18.5$ cm) are somewhat less accurate than those obtained from nearer particle fields ($L = 6.5$ cm). This could be attributed to the difference in the Fresnel number [15].

In general the step size in the z-depth direction for sampling the sharpness profile, $S(z)$, is selected to be less than 5 times the initially determined mean particle diameter, in order that the valid peaks are well resolved. A bigger step size reduces the resolution of the sharpness profile, whereas a smaller step size increases the computational time. Here, in the processing of the 1024×1024 synthetic hologram of 287 particles, the step size is chosen to be 0.5 mm for a depth range of 6 cm, corresponding to 120 z-planes.

In total it takes about 8 h for a computer with a 2.1 GHz CPU (Intel i7-3612QM) to run the refinement algorithm on one hologram. Among the processing steps, the computation of sharpness profiles for each particle is the most time-consuming. In general, the work reported here has not been focused on minimizing the processing time, and many opportunities for improvement likely exist. For example, GPU processing could be leveraged [5]. Also, further investigation is warranted to determine the optimum number of z-planes in the depth search as well as the number of thresholds used to determine the optimum threshold.

B. Application to Experimental Calibration Holograms

The experimental configuration to capture calibration holograms is shown in Fig. 7(a). Spherical particles are dispersed in silicone oil contained in an optical-glass cuvette. The inner dimensions of the cuvette are 5 cm × 5 cm × 5 cm. The cuvette is placed on a translation stage, which provides uniform displacement of particles in the z direction. The collimated beam from a laser (Coherent Verdi V6, $\lambda = 532$ nm) illuminates the particle field, and the resultant hologram is recorded by a CCD camera. Calibration holograms are taken of two sets of particle fields, as shown in Fig. 7(b). Set "A" is similar to the synthetic particle field discussed in Subsection 4.A, and consists of two particle size classes (mean diameter ~115 μm and ~450 μm). Set "B" consists of relatively bigger particles whose mean diameter is approximately 450 μm. A pair of sequential holograms is obtained wherein the particle field is translated by 2 mm in the z direction between each recording. This imposes a known z-displacement on the particles, which can be compared to measured quantities. The hologram size is 1024×1024 for set "A" and 3248×4872 for set "B". The pixel size is 7.4 μm. Particles in consecutive holograms are measured using the hybrid method along with the refinement, and further paired to calculate the z-displacement, Δz_d. From all measured particle

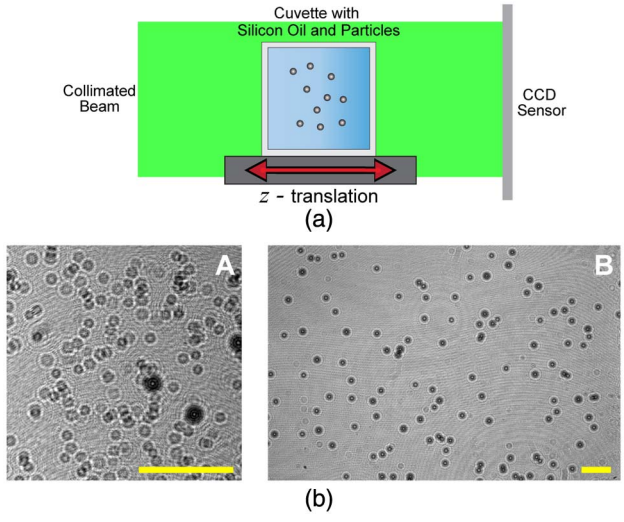

Fig. 7. (a) Experimental configuration to capture calibration holograms and (b) sample holograms of calibration particle fields, sets "A" and "B". The scale bars represent 3 mm.

Table 2. Performance and Improvement Achieved by the Refinement Applied to Experimental Calibration Holograms

		Set "A" $L \approx 4.6$ cm $\overline{F} \approx 0.088$ SD $\approx 4.0\%$	Set "B" $L \approx 17.0$ cm $\overline{F} \approx 0.452$ SD $\approx 2.7\%$
Number of false particle N_f		39	15
Identification effectiveness R_i		89.7%	86.7%
Separation effectiveness R_s		88.9%	76.9%
Mean displacement Error (μm)	$\lvert\overline{\Delta z_d} - \Delta z_0\rvert$	82	101
	$\lvert\overline{\Delta z_d} - \Delta z_0\rvert'$[a]	22	6
Relative depth Uncertainty	$\delta_z/\overline{D_d}$	11.8	1.56
	$\delta'_z/\overline{D'_d}$	0.72	0.47
Mean particle Diameter (μm)	$\overline{D_d}$	129	455
	$\overline{D'_d}$	119	446

[a]The prime signifies quantities obtained after refinement.

pairs, the mean measured displacement, $\overline{\Delta z_d}$, and the standard deviation of measured displacements are calculated. The approach used to evaluate the mean displacement error, $|\overline{\Delta z_d} - \Delta z_0|$, and the relative depth uncertainty, $\delta_z/\bar{D}_d$, is identical to that described in [15]. Here, the standard deviation of displacements detected from all pairs of particles is divided by $2^{1/2}$ in order to yield an estimate of depth uncertainty, δ_z. The discrepancy between the mean displacement, $\overline{\Delta z_d}$, and the actual displacement, Δz_0 (2 mm), is the error of mean displacement.

The total number of false particles, N_f, in experimental verification is manually determined by examining the initially detected particles obtained from the hybrid method. The performance of the refinement applied to experimental calibration holograms is summarized in Table 2. Consistent with the results obtained from synthetic holograms, about 90% of the false particles are identified, and the majority of identified false particles are successfully separated. The effect of refinement on measurement accuracy is demonstrated by the improvement of z-displacement measurement, also shown in Table 2. After refinement the mean displacement is measured more precisely. In addition, the depth uncertainty (standard deviation of displacements divided by $2^{1/2}$) is reduced dramatically to 0.72 mean particle diameters for set "A". Set "B" is a relatively sparse particle field; nevertheless, the few false particles severely affect the overall accuracy of displacement measurement, which is indicated by the significant reduction in depth uncertainty after those particles are detected and separated.

C. Practical Applications to Liquid Breakup

Holograms are taken of aerodynamic breakup of a single drop [9] and drop impact on a thin film [10]. In both cases, improvement in measurement accuracy is demonstrated qualitatively via comparison of droplet velocity vectors obtained before and after refinement.

The DIH setup to characterize aerodynamic fragmentation of a drop is shown in Fig. 8(a) [9].

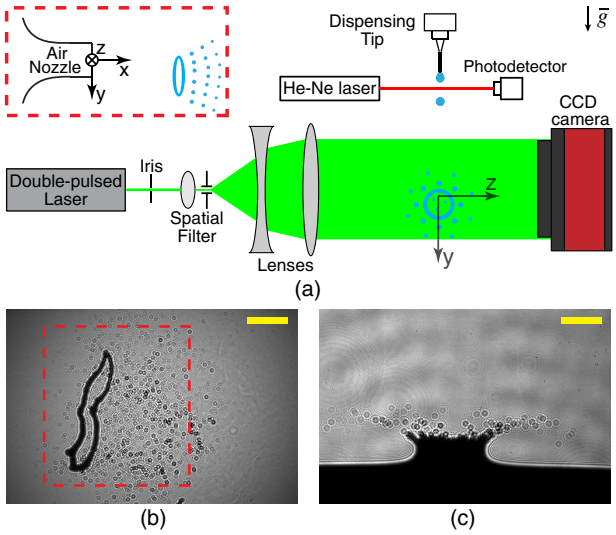

Fig. 8. (a) Experimental DIH setup for characterization of aerodynamic breakup of a single drop and (b) a sample hologram. (c) A sample hologram taken of drop impact on a thin film. Inset in (a): air nozzle viewed from the z direction. The scale bars represent 5 mm.

Sequential holograms with known time intervals are recorded by a CCD camera synchronized with a double-pulsed Nd:YAG laser. The air jet from a nozzle exerts aerodynamic forces on a falling drop, leading to the breakup of the drop, as shown in the inset in Fig. 8(a). An example hologram is shown in Fig. 8(b), where the encircled region is processed by the hybrid method to extract the particle information. Here, the minimum detectable diameter is set to 45 μm. Particles detected from two sequential holograms are paired to calculate the 3D displacement and velocity. The experimental setup to quantify drop impact on a thin film is similar to that in Fig. 8(a) [10], and a sample hologram of drop impact is shown in Fig. 8(c). Note, the coordinate origin for aerodynamic drop breakup is fixed at the center of the air nozzle outlet, whereas that of drop impact is attached to the center of the hologram plane.

Table 3. Performance of the Refinement Applied to Practical Holograms

	Aerodynamic Drop Fragmentation	Drop Impact
	$\overline{F} = 0.030$ SD = 2.2%	$\overline{F} = 0.036$ SD = 1.2%
Mean particle diameter $\overline{D_d}$ (μm)	108	157
Number of false particle N_f	197	6
Identification effectiveness R_i	72.1%	83.3%
Separation effectiveness R_s	60.6%	60%

The proposed refinement method is applied to results obtained from the hybrid method, and the results are quantified in Table 3. The slightly smaller identification effectiveness and separation effectiveness in the case of aerodynamic fragmentation can be attributed to the fact that the refinement, like the hybrid method, relies on the analysis of edge sharpness and performs relatively better for bigger particles, whereas the size distribution of droplets due to bag breakup peaks at a small diameter [9].

The velocity fields obtained with and without the refinement for the aerodynamic breakup case are shown in Fig. 9. Since a false particle typically contains more than one particle, it is characterized by excessive size. After refinement excessively big particles are eliminated. Further, separation of false particles results in an increase in the number of retrieved vectors. Figures 9(b) and 9(c) show the velocity fields viewed from the x-direction. The mean and standard deviation of droplet velocities in the four quadrants, divided according to the center of the rim, are also shown. The mean relative y-velocities obtained without the refinement are similar to those obtained with the refinement. However, the difference in mean z-velocities is more significant. Physically, the droplet distribution and motion are expected to be approximately symmetric with respect to the center of the rim, and thus the standard deviation of z-velocities is expected to be similar to

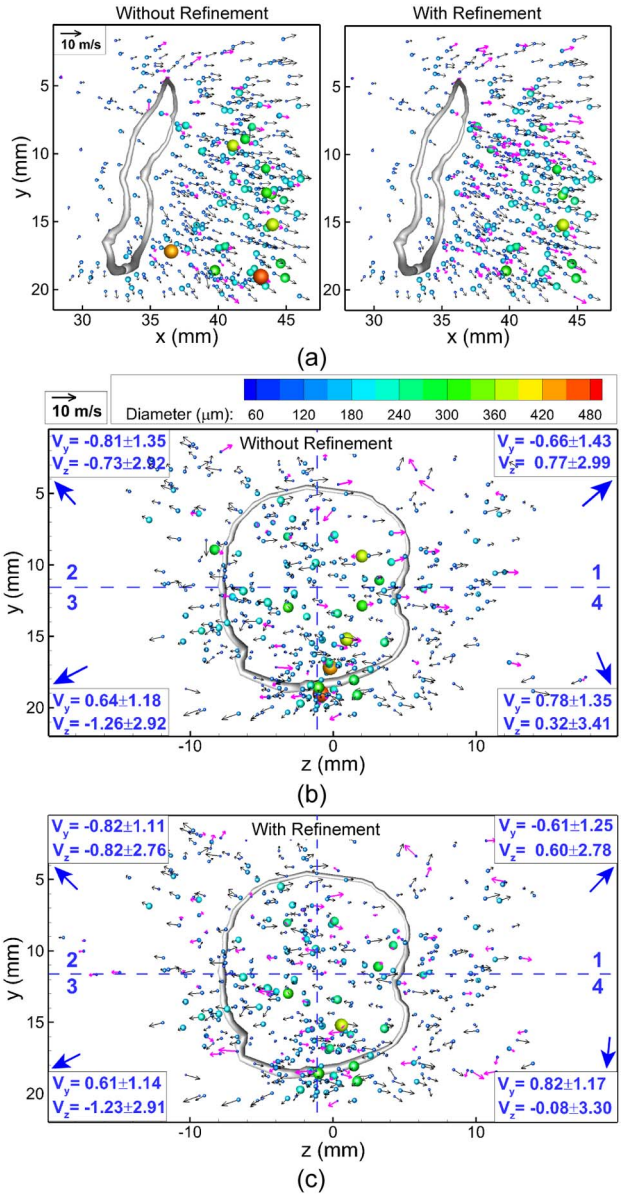

Fig. 9. Droplet velocity vectors of aerodynamic drop fragmentation measured with and without the refinement. (a) Comparison of in-plane (x–y) velocity vectors, (b) velocity vectors extracted without the refinement viewed from the x direction, (c) velocity vectors extracted with the refinement viewed from the x direction. Note that relative velocities with respect to the rim, i.e., $V = V_{\text{drop}} - V_{\text{rim}}$, are plotted in (b) and (c). V_y and V_z are the mean relative velocities in the y and z directions of the droplets in the four quadrants. The blue arrows show the directions of the mean relative velocities. The magenta vectors are those obtained from false particles and the corresponding refined particles.

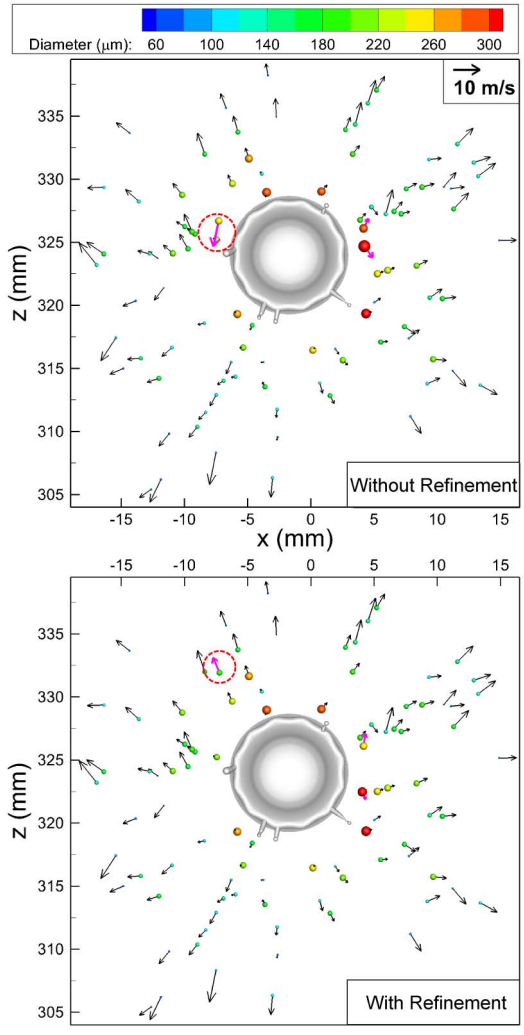

Fig. 10. Droplet velocity vectors produced by drop impact extracted with and without the refinement. The magenta vectors are those obtained from false particles and the corresponding refined particles.

that of the y-velocities. After refinement the standard deviations of z-velocities decrease slightly, which is indicative of some improvement in z-velocities. However, it should be noted that this improvement is still minor compared to the overall discrepancy between the standard deviation of y-velocities and that of z-velocities. It is well known that DIH measurement uncertainty is greater along the optical depth (z-direction). While the refinement procedure improves the results by eliminating grossly inaccurate vectors, it does not eliminate the depth of focus challenges [23].

Finally, the particle field in the drop impact experiment is sparse, so only a few false particles are identified and corrected, as shown in Fig. 10. Assuming radial spatial distribution and radial velocity of droplets with respect to the center of the crown, the effect of the refinement is exemplified by the encircled particle, whose position and velocity is improved.

5. Conclusions

One important application of DIH is particle field measurement, where simultaneous particle sizing and tracking is often desired. A major source of error in these applications is the measurement of transversely adjoining (overlapping) particles as single false particles. A few methods have been proposed to correct false particles in DIH. However, little is known about the performance of these methods, particularly their effects on measurement accuracy.

In the present study, a refinement procedure, for use in conjunction with the hybrid method [20], is proposed to diagnose and separate false particles. Like the hybrid method [15], the refinement is favorable for relatively large particles, whose diameter is much greater than the pixel size. The performance of the refinement is characterized via simulated and experimental holograms of 3D particle fields. On average, for a randomly distributed particle field, approximate 80% of false particles are identified and the majority are successfully separated. The significance of the refinement is demonstrated by improved accuracy in particle size, 3D position, and displacement measurements.

The authors would like to thank Edward Jimenez from Sandia National Laboratories for a thorough review of the manuscript. This work was supported by the Laboratory Directed Research and Development program at Sandia National Laboratories. Sandia is a multiprogram laboratory operated by Sandia Corporation, a Lockheed Martin Company, for the United States Department of Energy's National Nuclear Security Administration under contract DE-AC04-94AL85000.

References

1. H. Meng, G. Pan, Y. Pu, and S. H. Woodward, "Holographic particle image velocimetry: from film to digital recording," Meas. Sci. Technol. **15**, 673–685 (2004).
2. J. P. Fugal, R. A. Shaw, E. W. Saw, and A. V. Sergeyev, "Airborne digital holographic system for cloud particle measurements," Appl. Opt. **43**, 5987–5995 (2004).
3. T. Khanam, M. N. Rahman, A. Rajendran, V. Kariwala, and A. K. Asundi, "Accurate size measurement of needle-shaped particles using digital holography," Chem. Eng. Sci. **66**, 2699–2706 (2011).
4. N. A. Buchmann, C. Atkinson, and J. Soria, "Ultra-high-speed tomographic digital holographic velocimetry in supersonic particle-laden jet flows," Meas. Sci. Technol. **24**, 024005 (2013).
5. L. Tian, N. Loomis, J. A. Domínguez-Caballero, and G. Barbastathis, "Quantitative measurement of size and three-dimensional position of fast-moving bubbles in air-water mixture flows using digital holography," Appl. Opt. **49**, 1549–1554 (2010).
6. D. Lebrun, D. Allano, L. Méès, F. Walle, F. Corbin, R. Boucheron, and D. Fréchou, "Size measurement of bubbles in a cavitation tunnel by digital in-line holography," Appl. Opt. **50**, H1–H9 (2011).
7. Y. Yang and B. S. Kang, "Digital particle holographic system for measurements of spray field characteristics," Opt. Laser Eng. **49**, 1254–1263 (2011).
8. F. Lamadie, L. Bruel, and M. Himbert, "Digital holographic measurement of liquid-liquid two-phase flows," Opt. Laser Eng. **50**, 1716–1725 (2012).
9. J. Gao, D. R. Guildenbecher, P. L. Reu, V. Kulkarni, P. E. Sojka, and J. Chen, "Quantitative, three-dimensional diagnostics of multiphase drop fragmentation via digital in-line holography," Opt. Lett. **38**, 1893–1895 (2013).
10. D. R. Guildenbecher, L. Engvall, J. Gao, T. W. Grasser, P. L. Reu, and J. Chen, "Digital in-line holography to quantify secondary droplets from the impact of a single drop on a thin film," Exp. Fluids **55**, 1–9 (2014).
11. J. Sheng, E. Malkiel, J. Katz, J. Adolf, R. Belas, and A. R. Place, "Digital holographic microscopy reveals prey-induced changes in swimming behavior of predatory dinoflagellates," Proc. Natl. Acad. Sci. USA **104**, 17512–17517 (2007).
12. Y.-S. Choi and S.-J. Lee, "Three-dimensional volumetric measurement of red blood cell motion using digital holographic microscopy," Appl. Opt. **48**, 2983–2990 (2009).
13. Y. Wu, X. Wu, Z. Wang, L. Chen, and K. Cen, "Coal powder measurement by digital holography with expanded measurement area," Appl. Opt. **50**, H22–H29 (2011).
14. J. W. Goodman, *Introduction to Fourier Optics* (McGraw-Hill, 1996).
15. J. Gao, D. R. Guildenbecher, P. L. Reu, and J. Chen, "Uncertainty characterization of particle depth measurement using digital in-line holography and the hybrid method," Opt. Express **21**, 26432–26449 (2013).
16. D. Guildenbecher, P. L. Reu, J. Gao, and J. Chen, "Experimental methods to quantify the accuracy of 3D particle field measurements via digital holography," in *Digital Holography and Three-Dimensional Imaging* (Optical Society of America, 2013), paper DTh4A.2.
17. A. E. Mallahi and F. Dubois, "Separation of overlapped particles in digital holographic microscopy," Opt. Express **21**, 6466–6479 (2013).
18. N. Malpica, C. O. de Solrzano, J. J. Vaquero, A. Santos, I. Vallcorba, J. M. Garca-Sagredo, and F. del Pozo, "Applying watershed algorithms to the segmentation of clustered nuclei," Cytometry **28**, 289–297 (1997).
19. R. Fabbri, L. D. F. Costa, J. C. Torelli, and O. M. Bruno, "2D Euclidean distance transform algorithms: a comparative survey," ACM Comput. Surv. **40**, 1–44 (2008).
20. D. R. Guildenbecher, J. Gao, P. L. Reu, and J. Chen, "Digital holography simulations and experiments to quantify the accuracy of 3D particle location and 2D sizing using a proposed hybrid method," Appl. Opt. **52**, 3790–3801 (2013).
21. J. Y. Kim, J. H. Chu, and S. Y. Lee, "Improvement of pattern recognition algorithm for drop size measurement," Atomization Sprays **9**, 313–329 (1999).
22. M. Malek, D. Allano, S. Coëtmellec, and D. Lebrun, "Digital in-line holography: influence of the shadow density on particle field extraction," Opt. Express **12**, 2270–2279 (2004).
23. J. Katz and J. Sheng, "Applications of holography in fluid mechanics and particle dynamics," Annu. Rev. Fluid Mech. **42**, 531–555 (2010).